NJC

COMMUNICATION

View Article Online
View Journal

Cite this: DOI: 10.1039/d4nj03942d

Received 7th September 2024,
Accepted 4th November 2024

DOI: 10.1039/d4nj03942d

rsc.li/njc

Molten aluminum-doped porous silicon anodes enable high initial coulombic efficiency and stability†

Xiangshun Yan,[ab] Yuan Chen,[*a] Yongshu Wang,[ab] Fan Wu,[ab] Wensheng Wang,[ab] Wei Zhang,[ab] Xin Yang,[b] Zhongchao Bai,[a] Chao Dong,[c] Antonio Moore[d] and Qiang Zhang[a]

Aluminum-doped porous silicon was produced by a molten salt reaction. It showed accelerated lithium-ion diffusion kinetics and excellent structural stability. The pSi–Al significantly reduced the charge/ion transport resistance and first lithium capture by Al doping. It also affected the generation of the SEI during cycling and promoted the formation of LiF. The achieved ICE was 90.57% and the initial reversible capacity was 2860 mA h g^{-1}. Moreover, the reversible capacity was 1765 mA h g^{-1} after 100 cycles at 1 A g^{-1}, which demonstrated good electrochemical performance.

Introduction

The silicon-based anodes have drawn much attention in high energy density lithium ion batteries (LIBs).[1–3] However, the severe volume expansion, low conductivity, low Li^+ diffusion coefficients, and excessive depletion of the Li source[4–7] lead to poor stability and low ICE (65–85%).[8,9] Therefore, researchers have put much effort into enhancing the stability and ICE of silicon anodes.

To strengthen the stability, strategies include reducing the particle size and creating nanostructures, such as nanoparticles,[10] nanowires,[11] thin films,[12] and porous structures. Alternatively, surface coatings, composited with metal or carbon,[13,14] and pre-lithium[15] are usually employed. Additionally, nanoization and porosity can significantly reduce the material's volume expansion. For example, ant's nest porous silicon exhibited a reversible capacity of 1271 mA h g^{-1} at 2 A g^{-1}.[16] The three-dimensional interconnected nanostructure could effectively prevent particle pulverization and accommodate the volume expansion during cycling. It is known that the effect of Li capture in silicon anodes is responsible for around 30% of initial Li loss.[17] Therefore, the key to raising ICE is to reduce Li capture.

Moreover, the ICEs of silicon anodes are usually below 85%. Heteroatom doping was demonstrated to be an efficient route to improve the ICE, such as with phosphorus,[18] boron,[19] or metals.[20–22] For instance, Ma *et al.*[23] reported a molten salt alloying/dealloying method to prepare a 3D nanoporous silicon material (np-Si), which showed an ICE of 77.5% and a capacity retention of 83% after 1000 cycles. Xu *et al.*[24] developed Sn-doped Si (Sn–pSi), which showed an ICE of 84.3%, and a capacity of 1165 mA h g^{-1} after 400 cycles at 1 A g^{-1}. The Si@SiO_x/Ag reported by Zhang *et al.* showed an ICE of 89.7%, and an initial discharge capacity of 2919 mA h g^{-1} at 500 mA g^{-1}.[25] Doping could not only increase the conductivity, but also regulate the reaction kinetics, such as Li alloying and SEI growth.[24] Therefore, developing new ways to precisely regulate the atomic structure of silicon anodes is expected to achieve higher electrochemical performance. As the radius of Al was close to that of Si, substitution could not cause obvious lattice deformation.

In this work, we proposed a molten salt-assisted aluminum-doped and porous strategy to strengthen the conductivity and stability of the silicon anode. The pSi–Al anode exhibited enhanced lithium storage performance in terms of excellent cycling stability and rate performance.

Results and discussion

The synthesis steps of pSi–Al are illustrated in Fig. 1(a). The reaction is given in eqn (1).

$$3Mg_2Si + 4AlCl_3 \rightarrow 6MgCl_2 + 4Al + 3Si \quad (1)$$

The initial product was confirmed by X-ray diffraction (XRD) after water washing. It consisted of Al, Si, and un-reacted Mg_2Si

[a] College of Mechanical and Electronic Engineering, Shandong University of Science and Technology, Qingdao 266590, China. E-mail: chenyuan@sdust.edu.cn
[b] College of Energy Storage Technology, Shandong University of Science and Technology, Qingdao 266590, China
[c] Department of Chemistry and Physics, The University of Texas of the Permian Basin, 4901 E University Blvd, Odessa, TX 79762, USA
[d] Department of Life and Physical Sciences, Fisk University, 1000 17th Ave N, Nashville, TN 37208, USA

† Electronic supplementary information (ESI) available. See DOI: https://doi.org/10.1039/d4nj03942d

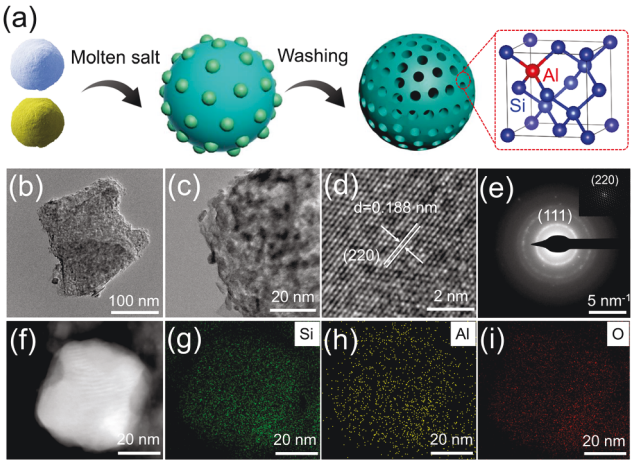

Fig. 1 (a) Synthesis illustration and crystal structure of pSi–Al. (b) and (c) TEM images of SA300. (d) HRTEM image of SA300. (e) SAED pattern and lattice puncta after FFT of SA300. (f) HAADF image of SA300. (g)–(i) Elemental mapping images of Si, Al, and O.

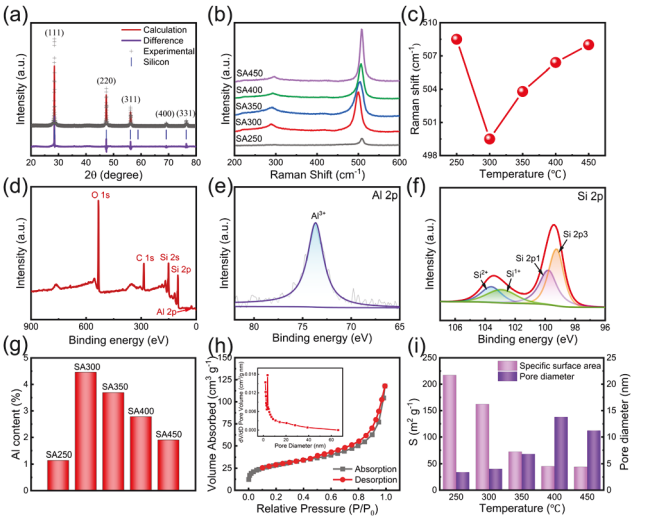

Fig. 2 (a) XRD pattern of SA300. (b) Raman patterns of pSi–Al. (c) Plot of the Raman peak changes. (d) XPS survey of SA300. (e) and (f) Al 2p and Si 2p high-resolution XPS spectra. (g) ICP results of Al content. (h) N_2 adsorption and desorption isotherm and pore diameter distribution curves. (i) Specific surface area and pore diameter statistics.

(Fig. S1, ESI†). Transmission electron microscopy (TEM) was used to examine the microstructure of pSi–Al (taking the 300 °C sample, named SA300). Fig. 1(b) and (c) display an abundant porous structure, which agrees with the scanning electron microscopy (SEM) images (Fig. S2(a) and (b), ESI†). The high-resolution TEM and selected area electron diffraction (SAED) results showed clear lattice stripes and diffraction rings (Fig. 1(d) and (e)). The lattice spacing measured at 0.188 nm (Fig. S2(c), ESI†). It was slightly smaller than the (220) crystal plane spacing of silicon. The distribution of lattice puncta of SA300 was obtained after the Fourier transform (Fig. 1(e), inset). The energy dispersive X-ray (EDX) spectroscopy results suggested that Si and Al were distributed uniformly throughout the whole particle (Fig. 1(f)–(i)). This indicated that Al had been successfully introduced into the lattice of Si.

The XRD results of SA300 are shown in Fig. 2(a). All of the peaks can be index to the Si standard card (JCPDS 27-1402). The obtained unit cell parameters were: a = 5.43024 Å, Vol. = 160.124 Å^3, density = 2.33 g cm^{-2}. Compared with the standard card (JCPDS 27-1402, where, a = 5.43088 Å, Vol. = 160.2 Å^3, density = 2.329 g cm^{-2}), SA300 had decreased lattice constant and volume. Meanwhile, the XRD results of pSi–Al are shown in Fig. S3(a) (ESI†) from 250 to 450 °C. The localized magnification of peak (111) showed that the position shifted to the right and then to the left as the temperature increased. The maximum shift was at 300 °C (Fig. S3(b), ESI†). The Raman spectra showed that the main vibration peaks derived from Si–Si bonds and the maximum deviation was at 300 °C (Fig. 2(b) and (c)), which indicated the highest doping content. The X-ray photoelectron spectroscopy (XPS) survey scan demonstrated that SA300 consisted of Si, Al, and O (Fig. 2(d)). The Al high-resolution spectrum peak located at 73.84 eV was obviously observed (Fig. 2(e)). The peaks for Si located at 103.59 eV, 102.9 eV, 99.76 eV and 99.23 eV could be attributed to Si^{2+}, Si^{1+}, and Si 2p, respectively (Fig. 2(f)). The accurate content of Al was confirmed by inductively coupled plasma mass spectrometry (ICP-MS) (Fig. 2(g)) and the maximum content was 4.46% for SA300. Furthermore, the content gradually decreased at temperatures over 300 °C, which agreed with the XRD and Raman results.

Fig. 2(h) displays the N_2 adsorption and desorption isotherms and the pore diameter distribution. A specific surface area of 162 m^2 g^{-1} and average pore diameter of 4.03 nm were presented for SA300. Meanwhile, specific surface areas of 217 m^2 g^{-1}, 72 m^2 g^{-1}, 45 m^2 g^{-1} and 44 m^2 g^{-1} were recorded for SA250, SA350, SA400, and SA450, respectively (Fig. 2(i)). However, the pore diameter showed the opposite tendency.

We have found that SA300 showed an ICE of 90.57%, while that of SA250 was 70% (Fig. 3(a) and (b)). Considering their similar porous structures, the significant difference in ICE derived from the Al doping content. To find the reason for the higher ICE, the mechanism was explored. Firstly, the volume expansion was investigated after the first cycle (Fig. S4(a)–(h), ESI†). No apparent crushing was found in both electrodes. The

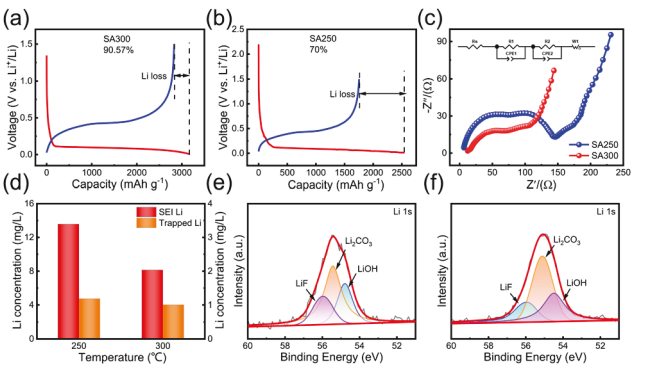

Fig. 3 Initial charge/discharge voltage profiles: (a) SA300; (b) SA250. (c) EIS of SA300 and SA250 after the first cycle. (d) SEI Li^+ and trapped Li^+ of SA300 and SA250. (e) Li 1s high-resolution XPS spectra of SA300. (f) Li 1s high-resolution XPS spectra of SA250.

thickness of SA300 was measured to range from 5.526 μm to 5.767 μm, while that of SA250 ranged from 7.048 μm to 7.392 μm. This meant that the initial Li loss was hardly due to volume expansion.

To ascertain the effect of the SEI, TEM was conducted. The thickness of the SEI was 19.17 nm and 19.62 nm for SA300 and SA250, respectively (Fig. S4(i) and (j), ESI†). Electrochemical impedance spectroscopy (EIS) was conducted to explore the growth of the SEI (Fig. 3(c)). The two high-frequency semicircles and the low-frequency slash represent the creation of the SEI, the charge transfer reaction at the electrode–electrolyte interface, and the Li^+ diffusion process, respectively. The fitted R_{SEI} values were 60.8 Ω and 65.9 Ω, respectively, which agreed with the TEM results (Fig. S4(i) and (j), ESI†). Therefore, the SEI formation did not exhibit significant differences.

Subsequently, Li capture was taken into consideration. The Li^+ concentrations in the SEIs of SA250 and SA300 were measured to be 13.57 mg L^{-1} and 8.136 mg L^{-1}, respectively (Fig. 3(d)). Meanwhile, the captured Li^+ concentrations were 1.184 mg L^{-1} and 1.004 mg L^{-1}. The Li^+ capture of SA300 decreased by 15.2% compared with SA250. The peak positions of SA250 and SA300 in the Li spectrum were different (Fig. 3(e) and (f)). This was due to the interaction between Al^{3+} and Li^+ of SA300 after Al doping. The peak position of SA300 was located at 55.35 eV, and that of SA250 was located at 55.08 eV, showing a 0.27 eV shift. It was found that the proportion of LiF in SA300 was higher than in SA250 after fitting. Therefore, Al doping could directly affect the formation of the SEI components during cycling, which was more favorable to the formation of LiF. This could effectively protect the SEI structure during cycling, which could greatly improve the cycling stability of porous silicon.

Cyclic voltammetry (CV) was used to explore the Li storage performance. It revealed three initial cycles with a scan rate of 0.1 mV s^{-1} and voltage from 0.01 to 1.5 V (Fig. 4(a)). The reduction peak was observed below 0.1 V during the first discharge. This corresponded to the creation of LixSi alloy, and the hardly distinguishable reduction peak indicated stable SEI formation and minimal capacity loss. Subsequently, a new reduction peak appeared at 0.17 V. Then, oxidation peaks appeared at 0.35 V and 0.52 V. Additionally, the location of the anodic and cathodic peaks remained almost the same. The steady increase in peak current suggested gradual activation of pSi–Al.[26] No peaks of Li–Al interaction emerged, indicating that Al doping mainly enhanced the conductivity.

The corresponding charging/discharging voltage profiles of SA300 at 100 mA g^{-1} are displayed in Fig. 4(b). A clear plateau appeared at 0.1 V during the first discharge. The initial capacity loss primarily occurred during SEI formation, which was accompanied by irreversible Li^+ capture and vanished in the subsequent processes. The Coulombic efficiency increased to 95% and 97% in the second and third cycle. The ensuing profiles nearly overlapped, indicating excellent reversibility.

The cycling performances of Si–Nps, SA300 and SA250 at 1.0 A g^{-1} were investigated (Fig. 4(c)), which showed reversible capacities of 1894 mA h g^{-1}, 2382 mA h g^{-1}, and 1424 mA h g^{-1}, respectively. In the fifth cycle, SA300 achieved a coulombic efficiency over 99%. Moreover, it retained a reversible capacity of 1765 mA h g^{-1} after 100 cycles. The outstanding cycling stability of pSi–Al without any carbon coating should be noted. At the same time, the Si–Nps underwent a rapid decay in capacity after 20 cycles. Fig. S5 (ESI†) compares the cycling performances of the materials at each temperature. Apparently, SA300 had improved cycling stability. The long-term cycling performance of SA300 is shown in Fig. S6 (ESI†). The reversible capacity remained at 835.4 mA h g^{-1} after 300 cycles at 1 A g^{-1}.

The rate performances of Si–Nps, SA300 and SA250 were also studied (Fig. 4(d)). The reversible capacities of SA300 from 0.1 A g^{-1} to 5 A g^{-1} were 2905 mA h g^{-1}, 2058 mA h g^{-1}, 1754 mA h g^{-1}, 1193 mA h g^{-1} and 607 mA h g^{-1}, respectively. SA250 exhibited 2544 mA h g^{-1}, 1489 mA h g^{-1}, 1206 mA h g^{-1}, 957 mA h g^{-1}, and 588 mA h g^{-1}. Si–Nps exhibited 2513 mA h g^{-1}, 1368 mA h g^{-1}, 643 mA h g^{-1}, 276 mA h g^{-1} and 4.2 mA h g^{-1}. The reversible capacities of SA300 and SA250 recovered to 2104 mA h g^{-1} and 1511 mA h g^{-1} when the current density returned to 0.1 A g^{-1}. This suggested superior structural stability of pSi–Al. The initial discharge capacity and ICE of pSi–Al are shown in Fig. 4(e) and SA300 had the highest ICE. The ICE and reversible capacity were compared with recent reports (Fig. 4(f)).[4,25,27–32]

To assess the Li^+ diffusion kinetics, the CVs of SA300 and SA250 with scan rates from 0.1 to 1 mV s^{-1} were taken (Fig. 5(a) and (b)), which showed similar redox peak shapes. The peak current progressively rose as the scan rate increased. The potential difference was small between the redox peaks, indicating less electrochemical polarization.[33] The Li^+ storage includes two aspects: Li^+ diffusion and capacitance, and the relationship between the peak current (i) and scan rate (v) can be described with eqn (2) and (3).[34]

$$i = av^b \quad (2)$$

$$\log i = \log a + b \log v \quad (3)$$

$$i(v) = k_1 v + k_2 v^{\frac{1}{2}} \quad (4)$$

SA300 and SA250 had the fitted b values of 0.9 and 0.82 (Fig. 5(c)), which indicated a co-controlled process. Furthermore, the capacity control mechanism can be determined using

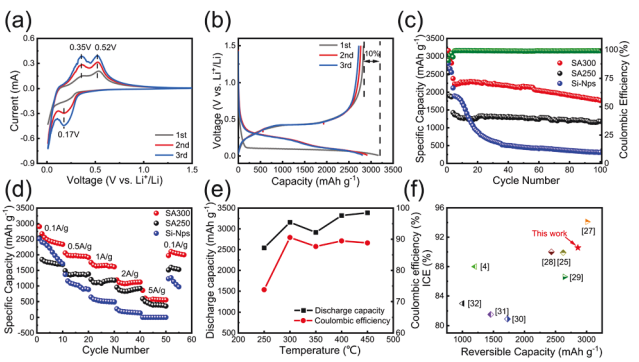

Fig. 4 (a) CV profiles of SA300 at 0.1 mV s^{-1}. (b) Charge/discharge voltage profiles of SA300 at 100 mA g^{-1}. (c) Cycling performance at 1.0 A g^{-1}. (d) Rate performance. (e) Comparison of pSi–Al materials. (f) Comparison of the ICE and reversible capacity of silicon anodes in the literature.

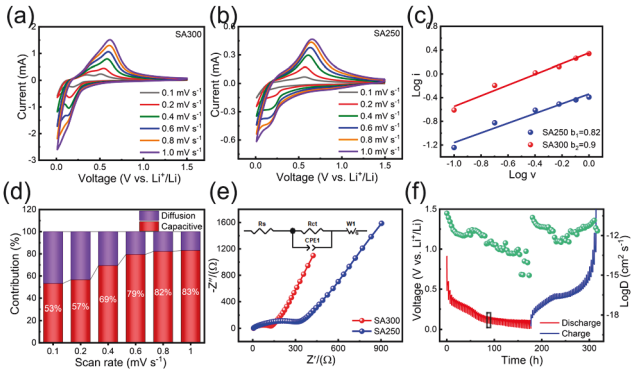

Fig. 5 CV profiles at various scan rates for (a) SA300 and (b) SA250. (c) Linear relationship between log i and log v for SA300 and SA250. (d) Capacitance and diffusion controlled contribution of SA300. (e) EIS comparison between SA300 and SA250 before cycling. (f) GITT profiles and calculated D of SA300.

eqn (4),[35] where $i(v)$ is the total current, and k_1v and $k_2v^{\frac{1}{2}}$ are the processes of the pseudocapacitance and diffusion-controlled contribution.[36] The pseudocapacitance contribution gradually increased as the scan rate increased (Fig. 5(d)). It reached 83% at 1.0 mV s^{-1} (Fig. S9(a), ESI†). The EIS results of SA300 and SA250 are displayed in Fig. 5(e) and Fig. S9(c) (ESI†). The fitted R_{ct} values before cycling were 112.4 Ω and 311.8 Ω. The R_{ct} values after 100 cycles were 86.9 Ω and 351.8 Ω. This further confirmed that Al doping significantly improved the conductivity. Moreover, the larger slope of the slash corresponded to faster Li^+ diffusion.[37,38] The EIS of the 100th and 200th cycles were also tested, and the R_{ct} values were 86.9 Ω and 133.4 Ω, respectively (Fig. S9(b), ESI†). This suggested that SA300 had substantially reduced charge transfer resistance and Li^+ diffusion coefficient.[39,40]

The galvanostatic intermittent titration technique (GITT) was performed and the Li^+ diffusion coefficient D was calculated using eqn (5):

$$D = \frac{4}{\pi\tau}\left(\frac{m_B V_M}{M_B S}\right)^2 \left(\frac{\Delta E_S}{\Delta E_\tau}\right)^2 \quad (5)$$

The obtained D of SA300 was 3.32×10^{-13} cm^2 s^{-1} to 2.33×10^{-11} cm^2 s^{-1} in the state of charge (Fig. 5(f) and Fig. S9(d), ESI†). The overpotential of SA300 was lower than that of SA250 (Fig. S9(e) and (f), ESI†).[41,42]

To confirm the structural integrity of the electrodes, the surface morphology was characterized using SEM. The SEM images of SA300 before and after 100 cycles are displayed in Fig. S10(a) and (b) (ESI†). It was observed that the electrode was still intact after cycling, although there was minor surface cracking. Moreover, the SEM of SA250 after cycling displayed noticeable alterations in the surface silicon particles, but no appreciable breaking was seen (Fig. S10(c) and (d), ESI†).

Conclusions

In conclusion, we have reported an Al-doped porous silicon anode. An improved ICE of 90.57% was achieved by reducing lithium capture. The maximum Al doping amount could be over 4% and the Li^+ capture decreased by 15.2% compared to SA250. Meanwhile, it promoted the formation of LiF during cycling, which demonstrated a stabilized SEI. A reasonably designed pSi–Al could effectively buffer the volume expansion, which gave accelerated Li^+ diffusion kinetics and excellent cycling stability. The electrochemical performance of pSi–Al was then enhanced by adjusting the reaction temperature to alter the Al doping amount. This strategy provided a new approach to improve the ICE of silicon-based materials.

Data availability

The data that support the findings of this study are available from the corresponding author upon reasonable request.

Conflicts of interest

There are no conflicts to declare.

Acknowledgements

This work was financially supported by the National Natural Science Foundation of China (No. 0203005790101), the Natural Science Foundation of Shandong Province (No. 02031010611, ZR2024QF273), and the National Science Foundation (No. 2246336).

References

1 G. G. Eshetu, H. Zhang, X. Judez, H. Adenusi, M. Armand, S. Passerini and E. Figgemeier, *Nat. Commun.*, 2021, **12**, 5459.
2 M. Jiang, J. Chen, Y. Zhang, N. Song, W. Jiang and J. Yang, *Adv. Sci.*, 2022, **9**, 2203162.
3 L. Sun, Y. Liu, R. Shao, J. Wu, R. Jiang and Z. Jin, *Energy Storage Mater.*, 2022, **46**, 482–502.
4 H. Tian, H. Tian, W. Yang, F. Zhang, W. Yang, Q. Zhang, Y. Wang, J. Liu, S. R. P. Silva, H. Liu and G. Wang, *Adv. Funct. Mater.*, 2021, **31**, 2101796.
5 X. Min, G. Xu, B. Xie, P. Guan, M. Sun and G. Cui, *Energy Storage Mater.*, 2022, **47**, 297–318.
6 Z. Cheng, H. Jiang, X. Zhang, F. Cheng, M. Wu and H. Zhang, *Adv. Funct. Mater.*, 2023, **33**, 01109.
7 Y. Zhang, B. Wu, G. Mu, C. Ma, D. Mu and F. Wu, *J. Energy Chem.*, 2022, **64**, 615–650.
8 R. Zhan, X. Wang, Z. Chen, Z. W. Seh, L. Wang and Y. Sun, *Adv. Energy Mater.*, 2021, **11**, 2101565.
9 C. Zu, H. Yu and H. Li, *InfoMat*, 2021, **3**, 648–661.
10 P. Li, J.-Y. Hwang and Y.-K. Sun, *ACS Nano*, 2019, **13**, 2624–2633.
11 G. Zhou, L. Xu, G. Hu, L. Mai and Y. Cui, *Chem. Rev.*, 2019, **119**, 11042–11109.
12 Y.-W. Cheng, C.-H. Chen, S.-A. Wang, Y.-C. Li, B.-L. Peng, J.-H. Huang and C.-P. Liu, *Nano Energy*, 2022, **102**, 107688.
13 K. Wang, S. Pei, Z. He, L.-A. Huang, S. Zhu, J. Guo, H. Shao and J. Wang, *Chem. Eng. J.*, 2019, **356**, 272–281.

14 Y. Tian, Y. An and J. Feng, *ACS Appl. Mater. Interfaces*, 2019, **11**, 10004–10011.
15 Z. Li, Y. Zhang, T. Liu, X. Gao, S. Li, M. Ling, C. Liang, J. Zheng and Z. Lin, *Adv. Energy Mater.*, 2020, **10**, 1903110.
16 W. An, B. Gao, S. Mei, B. Xiang, J. Fu, L. Wang, Q. Zhang, P. K. Chu and K. Huo, *Nat. Commun.*, 2019, **10**, 1447.
17 C.-Z. Ke, F. Liu, Z.-M. Zheng, H.-H. Zhang, M.-T. Cai, M. Li, Q.-Z. Yan, H.-X. Chen and Q.-B. Zhang, *Rare Met.*, 2021, **40**, 1347–1356.
18 L. Lin, Y. Ma, Q. Xie, L. Wang, Q. Zhang and D.-L. Peng, *ACS Nano*, 2017, **11**, 6893–6903.
19 H. Song, H. X. Wang, Z. Lin, X. Jiang, L. Yu, J. Xu, Z. Yu, X. Zhang, Y. Liu, P. He, L. Pan, Y. Shi, H. Zhou and K. Chen, *Adv. Funct. Mater.*, 2016, **26**, 524–531.
20 J. Lu, D. Li, L. Li, Y. Chai, M. Li, S. Yang and J. Liang, *J. Mater. Chem. A*, 2018, **6**, 5926–5934.
21 J. Zhou, H. Zhao, N. Lin, T. Li, Y. Li, S. Jiang, J. Tian and Y. Qian, *J. Mater. Chem. A*, 2020, **8**, 6597–6606.
22 Z. Xu, Y. Hou, J. Guo, J. Wang and S. Zhou, *ACS Appl. Energy Mater.*, 2021, **4**, 14141–14154.
23 Q. Ma, Y. Zhao, Y. Guo, Z. Zhao, H. Xie, P. Xing, D. Wang and H. Yin, *J. Mater. Chem. A*, 2022, **10**, 10004–10013.
24 J. Han, S. Jo, I. Na, S.-M. Oh, Y.-M. Jeon, J.-G. Park, B. Koo, H. Hyun, S. Seo, D. Lee, H. Kim, J. Kim, J.-C. Lim and J. Lim, *ACS Appl. Mater. Interfaces*, 2021, **13**, 52202–52214.
25 J. Zhang, S. Li, F. Xi, X. Wan, Z. Ding, Z. Chen, W. Ma and R. Deng, *Chem. Eng. J.*, 2022, **447**, 137563.
26 D. Rehnlund, F. Lindgren, S. Bohme, T. Nordh, Y. Zou, J. Pettersson, U. Bexell, M. Boman, K. Edstrom and L. Nyholm, *Energy Environ. Sci.*, 2017, **10**, 1350–1357.
27 B. Zhu, G. Liu, G. Lv, Y. Mu, Y. Zhao, Y. Wang, X. Li, P. Yao, Y. Deng, Y. Cui and J. Zhu, *Sci. Adv.*, 2019, **5**, eaax0651.
28 G. Hou, B. Cheng, Y. Yang, Y. Du, Y. Zhang, B. Li, J. He, Y. Zhou, D. Yi, N. Zhao, Y. Bando, D. Golberg, J. Yao, X. Wang and F. Yuan, *ACS Nano*, 2019, **13**, 10179–10190.
29 X. Zhang, D. Wang, X. Qiu, Y. Ma, D. Kong, K. Muellen, X. Li and L. Zhi, *Nat. Commun.*, 2020, **11**, 3826.
30 J. Shi, L. Zu, H. Gao, G. Hu and Q. Zhang, *Adv. Funct. Mater.*, 2020, **30**, 2002980.
31 Z. He, Z. Xiao, H. Yue, Y. Jiang, M. Zhao, Y. Zhu, C. Yu, Z. Zhu, F. Lu, H. Jiang, C. Zhang and F. Wei, *Adv. Funct. Mater.*, 2023, **33**, 00094.
32 C. Xu, L. Shen, W. Zhang, Y. Huang, Z. Sun, G. Zhao, Y. Lin, Q. Zhang, Z. Huang and J. Li, *Energy Storage Mater.*, 2023, **56**, 319–330.
33 D. Dai, X. Zhou, P. Yan, Z. Zhang, L. Wang, Y. Qiao, C. Wu, H. Li, W. Li, M. Jia, B. Li and D.-H. Liu, *ACS Appl. Mater. Interfaces*, 2024, **16**, 2428–2437.
34 J.-L. Yang, X.-X. Zhao, W. Zhang, K. Ren, X.-X. Luo, J.-M. Cao, S.-H. Zheng, W.-L. Li and X.-L. Wu, *Angew. Chem., Int. Ed.*, 2023, **62**, 2300258.
35 R. Yu, Y. Pan, Y. Liu, L. Zhou, D. Zhao, J. Wu and L. Mai, *ACS Nano*, 2023, 2c10381, DOI: **10.1021/acsnano.2c10381**.
36 J. Fei, S. Zhao, X. Bo, F. Xie, G. Li, E.-A. M. A. Ahmed, Q. Zhang, H. Jin and Z. Lin, *Carbon Energy*, 2023, **5**, 333.
37 J. Sun, B. Li, C. Jin, L. Peng, D. Dai, J. Hu, C. Yang, C. Lu and R. Yang, *J. Power Sources*, 2021, **484**, 229253.
38 K.-Y. Zhang, Y.-Q. Fu, H.-H. Liu, J.-L. Yang, M.-Y. Su, Y. Wang and X.-L. Wu, *Phys. Scr.*, 2023, **98**, 125977.
39 Y.-F. Meng, H.-J. Liang, C.-D. Zhao, W.-H. Li, Z.-Y. Gu, M.-X. Yu, B. Zhao, X.-K. Hou and X.-L. Wu, *J. Energy Chem.*, 2022, **64**, 166–171.
40 W. Huang, S. Liu, R. Yu, L. Zhou, Z. Liu and L. Mai, *Energy Environ. Mater.*, 2023, **6**, 12466.
41 S. Zhao, Y. He, Z. Wang, X. Bo, S. Hao, Y. Yuan, H. Jin, S. Wang and Z. Lin, *Adv. Energy Mater.*, 2022, **12**, 2201015.
42 S. Zhao, C. D. Sewell, R. Liu, S. Jia, Z. Wang, Y. He, K. Yuan, H. Jin, S. Wang, X. Liu and Z. Lin, *Adv. Energy Mater.*, 2020, **10**, 1902657.